Agricultural and Forest Meteorology 161 (2012) 46–56

Contents lists available at SciVerse ScienceDirect

Agricultural and Forest Meteorology

journal homepage: www.elsevier.com/locate/agrformet

Influence of canopy structure and direct beam solar irradiance on snowmelt rates in a mixed conifer forest

Keith N. Musselman[a,b,*], Noah P. Molotch[b,c], Steven A. Margulis[a], Peter B. Kirchner[d], Roger C. Bales[d]

[a] Department of Civil and Environmental Engineering, 5732 Boelter Hall, Box 951593, University of California, Los Angeles, CA 90095-1593, USA
[b] Institute of Arctic and Alpine Research and Department of Geography, 1560 30th Street, 450 UCB, University of Colorado, Boulder, CO 80309-0450, USA
[c] Jet Propulsion Laboratory, California Institute of Technology, Pasadena, CA 91109, USA
[d] Sierra Nevada Research Institute, University of California, 5200 North Lake Road, Merced, CA 95343, USA

ARTICLE INFO

Article history:
Received 27 July 2011
Received in revised form 27 February 2012
Accepted 19 March 2012

Keywords:
Forest
Canopy
Snow
SWE ablation
Direct beam transmissivity
Sky view factor

ABSTRACT

Sub-canopy snow ablation rates were measured for three years at forested research plots in the Sierra Nevada, California with a network of 24 automated snow depth sensors and monthly snow density surveys. Snow ablation rates, in mm SWE day^{-1}, specific to each depth sensor location were estimated as the seasonal maximum SWE divided by the number of days from peak SWE to snow disappearance. Estimates of sub-canopy direct beam solar irradiance and sky view factor (SVF_θ) derived from hemispherical photographs were used to explain the spatial distribution of snow ablation rates. Cumulative direct beam irradiance during the observed snowmelt periods explained the most variability in snow ablation rates for the most cloud-free melt season (58% in 2008; 4 cloudy days; at 15 sensor locations snowmelt duration ranged from 39 days to 88 days and direct irradiance ranged from 96 MJ m^{-2} to 603 MJ m^{-2}) and explained the least ablation variability for the cloudiest melt season of the study (29% in 2009; 23 cloudy days; at 12 sensor locations snowmelt duration ranged from 45 days to 79 days and direct irradiance ranged from 121 MJ m^{-2} to 410 MJ m^{-2}). Conversely, sky view factor (SVF_θ) explained the most variability in snow ablation rates under cloudier conditions (i.e. 87% in 2009) and the relationships were strongest when developed over the entire hemisphere (i.e. SVF_{90°, which ranged from 0.17 to 0.31). Combined, the two metrics studied here (sub-canopy direct beam irradiance and SVF_θ) may be used to explain much of the observed plot-scale variability in SWE ablation at finer time scales relevant to snow and hydrological model applications.

1. Introduction

It is estimated that ~19% of Northern Hemisphere snow cover overlaps forest vegetation (Rutter et al., 2009) and that fraction is higher in most mountainous regions where the majority of snow water resources accumulate. On the western slope of California's Sierra Nevada, greater than 40% of seasonally snow-covered land area at elevations >1220 m above sea level (asl) is forested (Kittredge, 1953). Conifer forest cover interacts with incident above-canopy atmospheric fluxes to form complex mosaics of net precipitation and energy at the sub-canopy surface. The physical mechanisms in forested environments that control gradients in snow interception, sublimation and throughfall (e.g. Hedstrom and Pomeroy, 1998; Koivusalo and Kokkonen, 2002; Lundberg et al., 1998; Storck et al., 2002), shortwave (e.g. Ellis and Pomeroy, 2007; Hardy et al., 2004; Pomeroy and Dion, 1996) and longwave (e.g. Essery et al., 2008b; Pomeroy et al., 2009) radiation, and the local advection of momentum, heat and moisture fluxes (e.g. Liston, 1995; Price and Dunne, 1976) are well documented. The heterogeneous arrangement of tree boles, branches, needles and understory together with micrometeorology and terrain dictate the physical processes listed above and ultimately govern the hydrology and ecology of many seasonally snow-covered forested catchments. Relative to open areas, a general dichotomy in forest – snow processes has been identified in which conifer canopy cover reduces the total annual meltwater available to runoff and/or infiltration through interception losses (Essery et al., 2003; Hedstrom and Pomeroy, 1998), while sub-canopy snow ablation processes determine the duration of snow cover and meltwater inputs (Link and Marks, 1999; Liston, 1995). The structure of vegetation, combined with seasonal variations in solar elevation and cloud cover, dictate the forest radiation regime (Baldocchi et al., 1984; López-Moreno and Stähli, 2008; Stähli et al., 2009). Whether forests become snow-free before or after nearby clearings is found to be a function of

* Corresponding author at: Institute of Arctic and Alpine Research, 1560 30th Street, 450 UCB, University of Colorado, Boulder, CO 80309-0450, USA.
Tel.: +1 1 520 820 3217.
E-mail address: musselman1@ucla.edu (K.N. Musselman).

0168-1923/$ – see front matter
doi:10.1016/j.agrformet.2012.03.011

latitude, forest structure, climate and seasonal meteorology (Faria et al., 2000; Molotch et al., 2011; Rutter et al., 2009; Schleppi, 2011; Sicart et al., 2004). Shade from solar radiation provided by forest cover has been shown to explain more than 60% of the variability in snowmelt rates between different stands of the same tree species (Talbot et al., 2006). As a result, the date of snow disappearance at the forested plot scale (i.e. 40 m × 40 m) can vary by as much as one month (Molotch et al., 2009) greatly impacting the magnitude of peak flows, the partition of meltwater to infiltration or runoff (Pomeroy et al., 2001) as well as seasonal soil moisture dynamics (Bales et al., 2011). The results imply that sub-canopy hydrometeorological surface fluxes and related states are well correlated with canopy cover 'upstream' of the prevailing flux paths. For example, the solar irradiance at a given sub-canopy location is most influenced by canopy configuration in the sky direction defined by the solar coordinates. Provided detailed canopy structure information, a consideration of the prevailing energy flux trajectories through a forest canopy may inform the derivation of optimal canopy metrics to improve energy flux parameterizations in canopy models.

Numerous empirical studies report correlations between snow properties and general descriptors of sub-canopy position relative to tree crowns such as 'open', 'edge', and 'under' categorizations (e.g. Musselman et al., 2008; Veatch et al., 2009). Others have compared snow depth or snow water equivalent (SWE) measured in canopy gaps of various sizes to that measured beneath the canopy (e.g. Golding and Swanson, 1986; Pomeroy et al., 2002). The results of these studies generally lack a pathway to predictive applications beyond the physiographic, climate, and weather conditions under which they were developed. A more detailed collection of canopy structure data in plot-scale studies permits an explicit evaluation of processes that influence snow ablation. In this regard, the objective of this study is to identify impacts of forest canopy structure and subsequent differences in direct beam solar irradiance on measured snow ablation. Two science questions are addressed: (1) Do canopy metrics derived from hemispherical photos explain observed spatial variability in snow ablation rates? and (2) Do optimal canopy metrics exist (either bulk or detailed descriptors) that can be used to explain observed variability in snow ablation rates?

2. Data and methods

Three years of seasonal SWE ablation as measured by a network of 24 ultrasonic snow depth sensors and manual snow density surveys were compared to: (1) photo-derived estimates of cumulative sub-canopy direct beam solar irradiance during the period of observed ablation; and (2) sky view factor (SVF_θ) computed over the full hemispherical range of zenith angles at one-degree increments. The direct beam irradiance, derived from detailed canopy transmissivity and above-canopy measurements, was used in explicit recognition that direct beam solar irradiance contributes

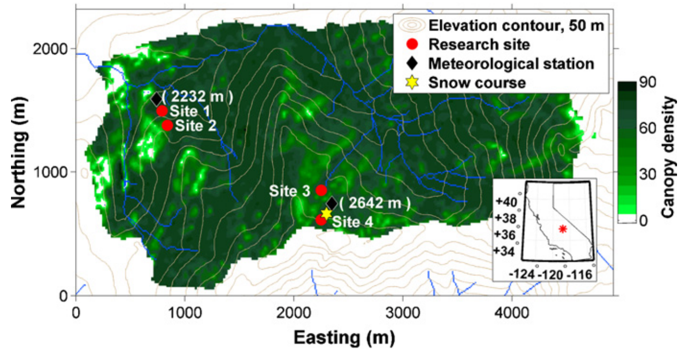

Fig. 1. The Wolverton basin in Sequoia National Park, California. Locations of the four instrumented research sites and two meteorological stations (elevation in meters asl) are indicated.

significantly to the spatial variability of the sub-canopy energy budget. The canopy metric SVF_θ was used in implicit recognition that the majority of above-canopy diffuse, longwave, and turbulent fluxes enters the canopy from all sky directions above the effective horizon, and may also hold information relevant to the estimation of terrestrial longwave fluxes. The analyses cover a range of elevation, slope, aspect and canopy configuration and three snow seasons (i.e. water years 2008–2010).

2.1. Study area

The study was conducted in the Wolverton basin, located in Sequoia National Park on the western slope of the southern Sierra Nevada, California, U.S.A. (36.59°N, 118.717°W) (Fig. 1). The Wolverton basin is a 7.22 km^2, snowmelt-dominated, forested watershed. Elevation ranges from 2192 m to 3075 m asl. Conifer forest stands include red fir (*Abiesmagnifica*), white fir (*Abiesconcolor*), Jeffrey pine (*Pinusjeffreyi*) and Lodgepole pine (*Pinuscontorta* subsp. *murrayana*). The forest is predominantly mature red fir, ranging in height from 20 to 50 m. The average canopy density is 65% and ranges from 0% in small clearings to 75% on steeper terrain with nearly continuous canopy coverage as determined from the National Land Cover Database (NLCD, 2001) (Homer et al., 2004) (Fig. 1). A monthly snow course has been conducted since 1925 by the California Cooperative Snow Survey (CCSS) at elevation 2622 m asl. The average April 1st SWE for the historic record is 932 mm. The average wind velocity measured during winter and spring at the upper elevation (2642 m asl) meteorological station (Fig. 1) for the three years of the study was 0.52 m s^{-1}, and the maximum daily wind velocity exceeded 3 m s^{-1} on only three occasions, indicating relatively little wind influence on local snow processes. In 2006, four extensively instrumented sets of sensor nodes (i.e. sites) were installed in the basin with locations stratified to represent the basin's range of aspect, elevation, and canopy cover (Table 1).

Table 1
Instrument site terrain and canopy statistics. The mean, maximum, and minimum values represent site variability sampled at locations of the six ultrasonic snow depth sensors.

	Elevation (m)	Aspect, degrees from north			Slope, degrees			Canopy openness[a]	SVF_{90°		
		Mean	Max.	Min.	Mean	Max.	Min.	1-[canopy density] NLCD, 2001	Mean	Max.	Min.
Site 1	2253	5	–	–	22	–	–	0.26	0.19	0.25	0.16
Site 2	2300	78.6	160	5	14.2	15	10	0.42	0.21	0.23	0.17
Site 3	2620	79	95	40	7.3	10	0	0.57	0.29	0.40	0.21
Site 4	2665	10	–	–	12.6	20	8	0.44	0.25	0.27	0.21

[a] Canopy openness is determined from Landsat-derived NLCD, 2001 canopy density. Site values represent the average canopy openness as sampled at the location of the six snow depth sensors at each site.

2.2. Hydrometeorological measurements

Six ultrasonic snow depth sensors (Judd Communications) were installed at four locations representing different elevations, aspects, and forest canopy characteristics (Table 1) following Molotch et al. (2009). The manufacturer specifies a senor range of 0.5–10 m and an accuracy of 1 cm or 0.4% of the target distance. Sensors at each site were separated by 8–55 m within the ~40 m × 40 m site footprint. Snow depth observations were recorded hourly and processed to remove outliers and fill gaps following Lehning et al. (2002) (Fig. 2).

Snow density data were obtained from five, six and four snow density surveys conducted in 2008, 2009 and 2010, respectively (Fig. 2). Snow density measurements at the four sites were obtained from approximately monthly (January–May) snow pits and CCSS snow course measurements. Snow pit density measurements made with 1000 cm^3 cutters were assumed to be representative of the plot-scale mean snow density. CCSS snow course density data represent the average of equally spaced Federal snow tube measurements made along multiple linear transects in close proximity to Sites 3 and 4 (Fig. 1). In cases where both snow pit and CCSS measurements were conducted within one week of each other, only the snow pit density measurements were used to maintain consistency and site representativeness. For each year, the timing of maximum SWE was determined by multiplying surveyed site-specific density values by sensor snow depth values corresponding to the respective survey dates. The survey date that yielded the highest sensor SWE at all sites was prescribed as the date of maximum annual SWE. Given an estimate of maximum SWE at each depth sensor location for each year of the study, an index of the seasonal SWE ablation rate was then computed as the maximum SWE at a given sensor divided by the number of days from maximum SWE until snow disappearance as recorded by the same sensor. The approach yielded an ensemble of seasonal SWE ablation indices corresponding to different canopy configurations, elevations, aspects, and slopes of the individual snow depth sensor locations.

Obtaining manual snow density measurements on the date of maximum SWE is complicated by weather and schedule constraints and slight differences in terrain and forest cover that may cause spatial heterogeneity in the timing of maximum SWE. Two assumptions were made in regard to maximum SWE accumulation. First, the timing of maximum SWE was assumed to be uniform across sensor locations in a given year; that is, the date (not the magnitude) of maximum SWE was assumed to be spatially invariant. This assumption was necessary because SWE was not explicitly measured at each sensor location, but estimated only when density observations were available. Second, it was assumed that, for each year, one of the monthly density surveys captured the snow density at the time of maximum SWE. This assumption was necessary because density measurements were made at monthly repeat intervals.

Measurements of hourly, global incident solar radiation ($R_{s\downarrow}$) unobstructed by surrounding forest canopy were not available in the forested Wolverton basin. Instead, $R_{s\downarrow}$ for the three years of the study were obtained from a meteorological station located above timberline at Topaz Lake in the Tokopah basin; 8 km ENE of the study site at 3220 m asl. The data were assumed to be representative of above-canopy $R_{s\downarrow}$ at the locations of the four sites. A four-day deployment of a Kipp and Zonen pyranometer in the Wolverton basin indicated cumulative differences with the Topaz Lake data of less than 4%. A three-year comparison of $R_{s\downarrow}$ measured at Topaz Lake and a station operated by the National Park Service 6 km WSW of the study site yielded a correlation coefficient of 0.93. Based on these two independent evaluations the use of Topaz Lake $R_{s\downarrow}$ measurements to represent above-canopy $R_{s\downarrow}$ in Wolverton is justified.

2.3. Hemispherical photography acquisition and analysis

An upward-looking hemispherical photograph was taken directly beneath each of the 24 depth sensors using a Nikon D700 digital single lens reflex camera (Nikon Corporation, Japan) with a Sigma 8 mm F3.5 EX DG Circular Fisheye Lens (Sigma Corporation, Japan). The camera was mounted on a tripod and photographs were taken at a height of 1.5 m, roughly consistent with the seasonal average snow depth at the study sites. A bubble level fitted to the lens cap ensured horizontal camera orientation and a compass was used to orient the top of the camera to true north following methods of Frazer et al. (2000) (Fig. 3a). The scientific image processing software Gap Light Analyzer (GLA) Version 2.0 (Frazer et al., 1999) was used to register and classify each digital hemispherical image following recommended methods of Frazer et al. (1999) and Hardy et al. (2004). The GLA image analysis created an image consisting solely of black and white pixels (Fig. 3b).

To characterize canopy structural parameters from a pre-processed hemispherical photo, an automated image analysis model was developed. The model first determines the image center and assigns Cartesian coordinates to each pixel, in number of pixels, with nadir specified as the central datum. The Cartesian coordinates are converted to a polar system such that each pixel is assigned a zenith angle (0 to $\pi/2$ radians) and an azimuth angle (0 to 2π radians) according to its position on the projected

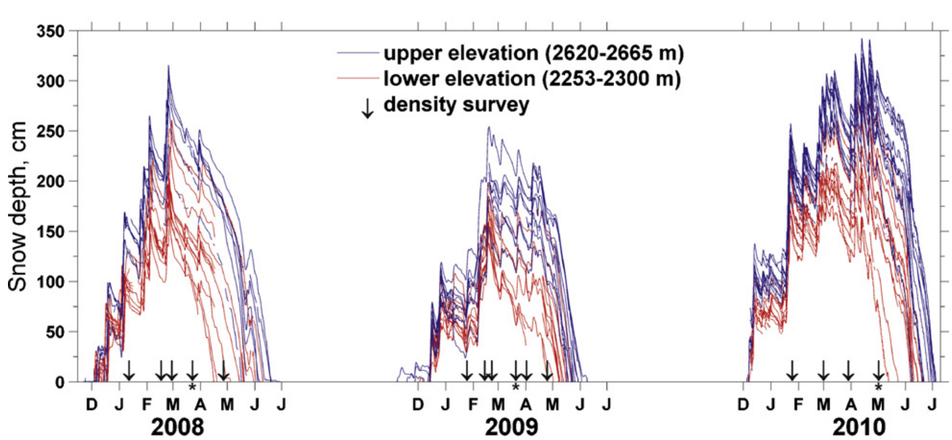

Fig. 2. Hourly snow depth recorded by 24 ultrasonic sensors at two lower (sites 1 and 2) and two upper (sites 3 and 4) research sites and neighboring meteorological stations for three years. Dates of 15 snow density surveys (↓ symbols) and the survey dates determined to coincide with the timing of annual maximum SWE (* symbols) are indicated.

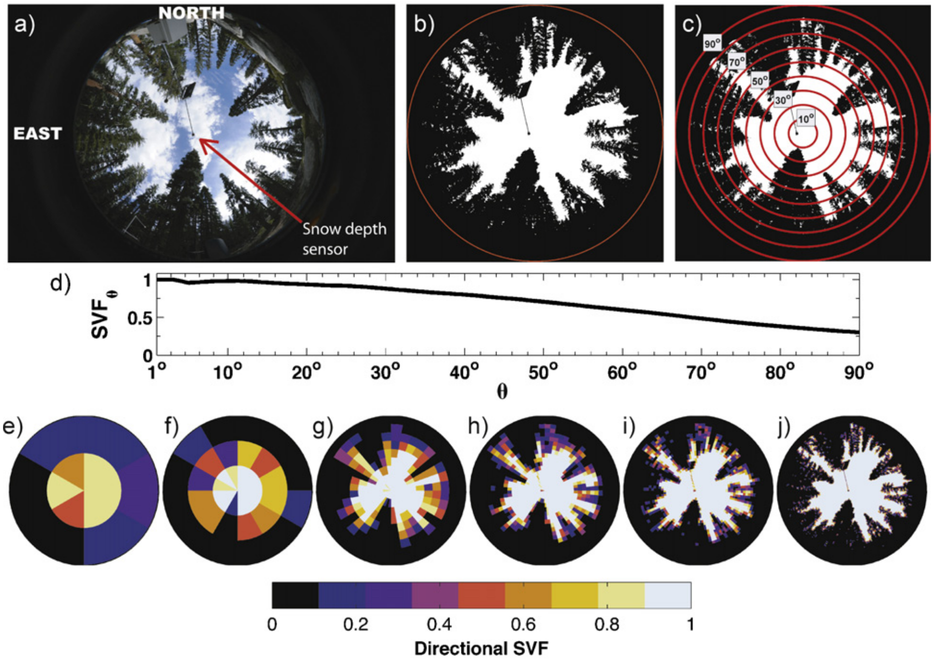

Fig. 3. Processing and analysis steps of a hemispherical canopy photograph including (a) a georeferenced digital hemispherical color photo (with location of the site 3, snow depth sensor #3 indicated), (b) binary pixel representation of the color photo with the circular exposure outlined, (c) photo with concentric circles defined by zenith angle, θ, (d) the resulting sky view factor (SVF_θ) determined by integrating fractional canopy openness from specified zenith angles at 1° increments (1–90°) to nadir (0°) and (e)–(j) examples of the hemispherical photo aggregated into discrete sky regions to determine directional SVF at (e) 12 sky regions or ~53°, (f) 36 sky regions or 30°, (g) 324 sky regions or 10°, (h) 1296 sky regions or 5°, (i) 3600 sky regions or 3°, and (j) 32,400 sky regions or 1° angular resolutions. (For interpretation of the references to color in this figure legend, the reader is referred to the web version of this article.)

hemisphere. The coordinate system is defined such that an azimuth angle of 0 radians and a zenith angle of $\pi/2$ radians refer to the circular exposure's topmost central pixel and the azimuth angle increases in a counter-clockwise fashion consistent with the orientation of an inverted plan view compass rose. The quality of the exposure's circular extent (~2000 × 2000 pixels) permits high resolution analysis. Radial projection errors are inherent to image acquisition. A five-piece polynomial was applied that adequately approximates the radial projection error provided by the lens manufacturer (Sigma Corporation, personal communication). Other sources of uncertainty associated with hemispherical photography include geo-reference errors and the subjectivity of RGB threshold specification.

2.4. Photo-derived canopy metrics

2.4.1. Sky view factor

Sky view factor (SVF_θ) was computed from binary hemispherical images as the weighted canopy openness over all azimuth angles (φ) from a specified zenith angle (θ) to nadir. The metric has been successfully used in the study of forest light environments (e.g. Hardy et al., 2004), longwave radiation (e.g. Essery et al., 2008b) and sub-canopy snow dynamics (e.g. López-Moreno and Latron, 2008). When computed over a single hemispherical region defined by θ, SVF_θ is a bulk, 0-D representation of canopy openness over a select concentric area of the projected hemisphere. When computed over a range of θ angles from 1° to 90°, SVF_θ becomes a one-dimensional array that describes the change in canopy openness as more of the surrounding forest is considered. Fig. 3c and d provide examples of SVF_θ computed at one-degree zenith angle increments over the field of view of a hemispherical photograph. In the example, SVF_θ is equal to one nearest nadir, decreases slightly as a result of the overhead snow depth sensor until an angle of ~12° is reached, beyond which canopy elements begin to enter the field of view and SVF_θ decreases more significantly (Fig. 3c and d). In this way, SVF_θ was computed for each hemispherical photo taken at depth sensor locations at one-degree intervals of θ from 1° to 90°.

2.4.2. Directional sky view factor

The explicit consideration of canopy openness as it might influence the direct beam solar flux entering the forest canopy in a specified trajectory is not achievable with bulk SVF_θ measurements. When computed over individual φ and θ ranges, however, SVF_θ gains a directional component (*directional SVF*) and becomes a two-dimensional (2-D) array that describes the hemispherical distribution of canopy openness relative to a photo location at any angular resolution of interest. Pre-processed hemispherical images were divided into circumferential and radial solid angles, or sky regions, specified by angular increments $\delta\theta_i$, and $\delta\varphi_j$. The total count and fraction of sky/non-sky pixels in each sky region were computed and binned in matrices of size $[2\pi/\delta\varphi_j, (\pi/2)/\delta\theta_i]$, representing weighting schemes and *directional SVF*, respectively. Fig. 3e–j illustrate examples of *directional SVF* computed over a specified range of φ and θ discretizations. An example in Fig. 3e shows the projected hemisphere divided into six φ and two θ bands for a total of 12 sky regions at an angular resolution of 60° (φ) and 45° (θ). In this study, the estimated total uncertainty in radial pixel position was one-degree. For this reason, a one-degree hemispherical angular resolution was chosen, representing 360 azimuth and 90 zenith discretizations or a total of 32,400 sky regions (Fig. 3j).

2.5. Canopy radiative transfer model

Directional SVF has been used extensively to estimate solar canopy transmissivity (e.g. Becker et al., 1989; Frazer et al., 2000; Hardy et al., 2004; Sicart et al., 2004). In this study, the sky coordinates of the sun were used to 'sample' the *directional SVF* from the sky region encompassing the sun's position. The sun's position in the sky at one-minute resolution was computed for the three years of the study following methods of Reda and Andreas (2004), with an uncertainty of ±0.0003°. A one-minute time scale was chosen to adequately capture the relative velocity (~0.25° per minute) of the sun's location on the projected hemispherical plane. Hourly measurements of above-canopy $R_{s\downarrow}$ were linearly resampled to one-minute estimates and used to estimate sub-canopy fluxes at the locations of hemispherical photos. Combined with one-degree resolution *directional SVF*, the one-minute time step captures the intermittent nature of sun flecks tracking on the forest floor and the resulting high temporal variability of the forest light environment. Differences in the physics of canopy attenuation/transmission of direct ($R_{s\downarrow dir}$) and diffuse ($R_{s\downarrow dif}$) solar radiation require these two components to be treated independently. The $R_{s\downarrow dir}$ and $R_{s\downarrow dif}$ fluxes were partitioned from the above-canopy global shortwave measurements using the all-sky solar partition model presented in Allen et al. (2006) as an empirical function of atmospheric transmissivity. The model provided one-minute estimates of above-canopy $R_{s\downarrow dir}$ and $R_{s\downarrow dif}$.

In this study, direct beam canopy transmissivity (*DBT*) is defined as the probability that the solar beam will pass through forest cover unimpeded by canopy elements at a given time and as determined at the location and height of a hemispherical photograph. *Directional SVF* sampled from sky regions corresponding to the track of the sun provided a high-resolution estimate of *DBT*. The model does not account for scattering of attenuated direct beam radiation. At every photo/depth sensor location, *directional SVF* and the trajectory of the sun in the sky were used to compute *DBT* for every minute of every day for the three water years of interest.

The one-minute detailed *DBT* was multiplied by the one-minute above-canopy $R_{s\downarrow dir}$ to estimate sub-canopy $R_{s\downarrow dir}$ on a horizontal plane. The direct beam irradiance estimated at the location of individual depth sensors was then projected on the local slope according to Oke (1988). The cumulative slope-projected direct beam irradiance calculated over the same time frame used to compute sensor-specific seasonal SWE ablation rates was used to test the correlation between the observed SWE ablation and estimated sub-canopy $R_{s\downarrow dir}$.

To evaluate the model's predictive accuracy of sub-canopy $R_{s\downarrow dir}$, canopy transmission of the above-canopy diffuse component was also estimated and the sub-canopy $R_{s\downarrow dir}$ and $R_{s\downarrow dif}$ fluxes were combined to represent the horizontal, sub-canopy global shortwave radiation. Estimates of sub-canopy $R_{s\downarrow}$ were then compared to pyranometer data. Unlike the source of the direct beam, which was treated as a point on the projected hemisphere, diffuse radiation may be transmitted from all sky regions. The anisotropic sky distribution of diffuse radiation was treated with a simple cosine approximation such that more weight was applied to the near-nadir sky regions (i.e. lower zenith angles) and less toward the horizon. Diffuse solar irradiance entering the canopy is absorbed, reflected, or transmitted. The fraction of unimpeded diffuse irradiance was determined by the *directional SVF* of each sky region. Reflection of the fraction of diffuse light incident on canopy elements (i.e. *1–directional SVF*) was approximated using an estimated canopy albedo and a Beer's-type exponential reduction as a function of effective leaf area index (*LAI′*). Photo-derived *LAI′* was computed following the gap fraction methods of Norman and Campbell (1989) and accounting for a sloped surface as Schleppi et al. (2007). The average *LAI′* from the 24 photos was 2.72 $m^2\,m^{-2}$ and the values ranged from 1.20 to 4.88 $m^2\,m^{-2}$. The sub-canopy $R_{s\downarrow dif}$ issuing from any sky direction was estimated as:

$$R_{s\downarrow sub\_dif_{i,j}} = R_{s\downarrow dif} \cos\theta_i (1 - SVF_{i,j})(1 - \alpha_c)\exp(-k \cdot LAI') \quad (1)$$

where k (–) is an extinction parameter typically between 0.4 and 0.8 and specified as 0.7, α_c is the conifer canopy albedo specified as 0.125, and $SVF_{i,j}$ is the *directional SVF* in the sky region defined by zenith angle i and azimuth angle j. An additional weighting scheme was necessary to account for the hemispherical effect of upper sky regions (i.e. solid angles) having less area than those nearer the horizon. Each sky region was assigned a weight defined as the pixel count for that region normalized by the total hemispherical pixel count. The weighted irradiance effectively permits all sky regions to contribute equally to the surface irradiance, computed as the summation of hemispherical weighted irradiance.

Model validation was conducted in two experiments. In the first experiment, upward-looking photographs were taken as close as possible to three mast-mounted pyranometers 3.5 m above the forest floor. The pyranometers logged data for eight days at one-minute resolution. In the second validation experiment, a total of nine leveled Kipp and Zonen pyranometers were deployed on the snow surface for three days in radial transects centered on a cluster of 40 m trees near Site 3. The sensors were programmed to log at five-minute intervals of ten-second integrated measurements. An additional, identically programmed pyranometer located in a large clearing ~0.5 km WSW of Site 1 provided 'above-canopy' radiation.

2.6. Regression analyses

Linear regression analyses were conducted on the relationships between measured seasonal SWE ablation rates at the 24 locations for three years and: (1) estimates of cumulative sub-canopy direct beam solar irradiance during the period of observed ablation; and (2) SVF_θ computed over the full hemispherical range of zenith angles at one-degree increments. The coefficient of determination (R^2), slope, intercepts and statistical significance (p-value) were evaluated.

3. Results

3.1. Hydrometeorological observations

Hourly time series of snow depth measured by the 24 ultrasonic sensors for water years 2008, 2009, and 2010 show that accumulation and depletion rates varied between upper (Sites 3 and 4; 2620–2665 m asl) and lower (Sites 1 and 2; 2253–2300 m asl) elevations, between sites at similar elevations, and between sensor locations at individual sites (Fig. 2). On average, the 12 sensors at the two lower elevation sites recorded seasonal maximum snow depths of 203 cm, 154 cm, and 199 cm for the three years, respectively, while the 12 sensors at the two upper elevation sites recorded average maximum depths of 278 cm, 194 cm, and 307 cm for the same years. The lower elevation sites accumulated 73%, 79%, and 65% of the average maximum snow depth at the upper elevation research sites for 2008, 2009, and 2010, respectively. Maximum snow depth was recorded on 26 February, 2008; 19 February, 2009; and 21 April, 2010 and the dates did not vary by elevation. Snow density data (not shown) from each of the three years exhibited a seasonal increase with the springtime maximum snowpack densities between 450 $kg\,m^{-3}$ and ~500 $kg\,m^{-3}$. The timing of seasonal maximum SWE was estimated to coincide with density surveys conducted on 23 March, 2008; 21 March, 2009; and 2 May, 2010 (Fig. 2, Table 2). Average maximum annual SWE for lower and upper elevation sites, respectively, was 519 mm and 955 mm in 2008; 263 mm and 576 mm in 2009; and 817 mm and 1330 mm in 2010. The melt season duration, defined as the number of days between peak SWE and snow disappearance, was found to vary significantly by site, year, and lower (sites 1 and 2) and upper (sites 3 and 4) elevations (Table 2).

Table 2
Melt season metrics.

Year	Date of peak SWE	Mean snow disappearance date				Melt season duration, days [min., mean, max.]			
		Site 1	Site 2	Site 3	Site 4	Site 1	Site 2	Site 3	Site 4
2008	March 23	May 24	May 2	May 29	June 14	[57, 62, 70]	[25, 40, 57]	[56, 70, 83]	[76, 84, 88]
2009	March 21	May 10	May 3	May 25	May 30	[41, 50, 57]	[29, 43, 53]	[58, 66, 79]	[64, 70, 75]
2010	May 2	June 13	May 30	June 18	July 1	[39, 43, 49]	[11, 29, 39]	[37, 47, 64]	[56, 61, 64]

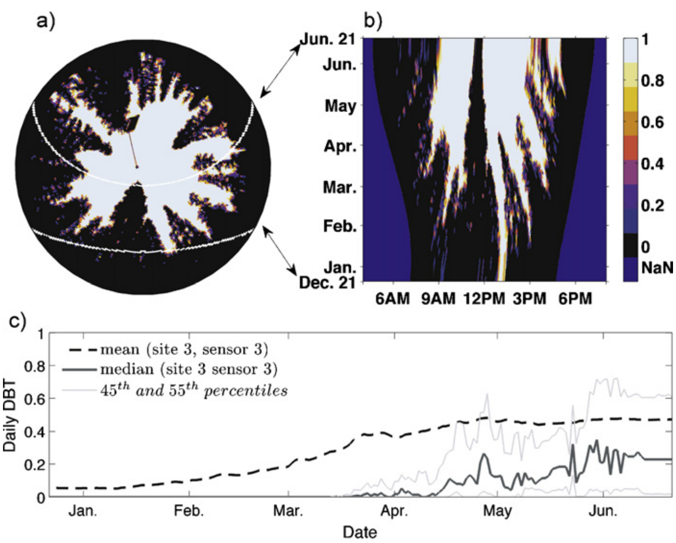

Fig. 4. Directional SVF at one-degree angular resolution at the same depth sensor location as in Fig. 3 showing (a) the projected solar disk trajectory on the winter (lower) and summer (upper) solstices, (b) directional SVF sampled along the sun track (i.e. direct beam canopy transmissivity, DBT) at one-minute (x-axis) resolution for every day (y-axis) between the solstices, and (c) the seasonal variability including the mean, median, and the 45th and 55th percentiles of the daily mean DBT at the same location.

3.2. Direct beam canopy transmissivity (DBT)

The *DBT* at the location of snow depth sensor #3, site #3 is illustrated in Fig. 4a and b. In the example, *directional SVF* is sampled along the solar disk trajectory (Fig. 4a) at one-minute resolution between the hours of 4:00 and 20:00 PST for every day between the winter and summer solstices (Fig. 4b). The daily (i.e. when the sun is above the horizon) mean *DBT* for this location (Fig. 4c) has a seasonal minimum of 0.05 on 11 January, a seasonal maximum of 0.48 on 29 April, and the seasonal average of the mean daily *DBT* is 0.29. However, the high variability of the one-minute *DBT* is not well represented by the seasonal evolution of the daily mean as indicated by the near-zero median and 45th and 55th percentiles for much of the year (Fig. 4c). The distribution of minutes when direct sunlight passes unimpeded through the canopy (i.e. $DBT = 1$) is heavily skewed toward solar noon (at the daily scale) and the summer solstice (at the seasonal or annual scale), but that general trend is dependent on location and surrounding forest structure. For example, the spatial variability of the seasonal distribution of daytime *DBT* computed between the solstices as in Fig. 4b but at all 24 photo/snow depth sensor locations is illustrated in Fig. 5a. The mean of the daily average *DBT* at all sensor locations varies from 0.044 to 0.32 between the winter and summer solstices, respectively (Fig. 5b). The 24-sensor mean of the photo-derived *DBT* (0.19) is only slightly less than the photo-derived 24-sensor mean SVF_{90° (0.24; Table 1) – a surprising result given that SVF_{90° contains information about a much larger portion of the projected hemisphere than the angular swath defined by the solar coordinates. However, particularly at time scales greater than one hour, the mean *DBT* does not correspond to sub-canopy potential direct beam irradiance without consideration of the highly variable nature of above-canopy solar radiation. In the analyses to follow, the photo-derived *DBT* was used to explicitly estimate sub-canopy direct beam solar irradiance in an effort to capture the highly dynamic nature of the sub-canopy shortwave environment.

3.3. Above-canopy radiation

Hourly measured above-canopy $R_{S\downarrow}$ data for the three years are shown in Fig. 6; the darker horizontal bands indicate cloud cover (Fig. 6). A daily clearness index, K_τ (Liu and Jordan, 1960) (Eq. (2)),

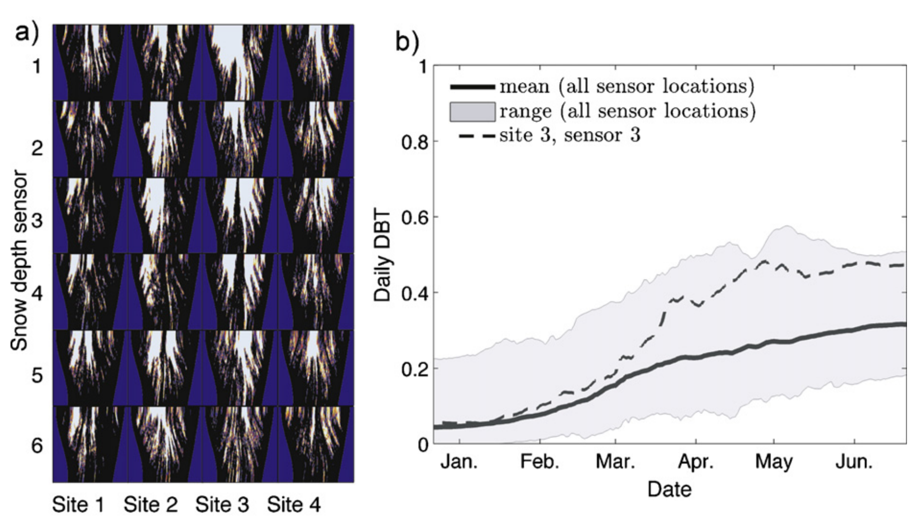

Fig. 5. Direct beam canopy transmissivity (DBT) between the winter and summer solstices (a) for all daylight hours as shown in Fig. 4 but at the locations of all 24 snow depth sensors, and (b) as the sensor network mean (solid line) and range (shading) of the daily average at all sensor locations and relative to the site 3, sensor 3 mean DBT (dashed line) shown in Fig. 4.

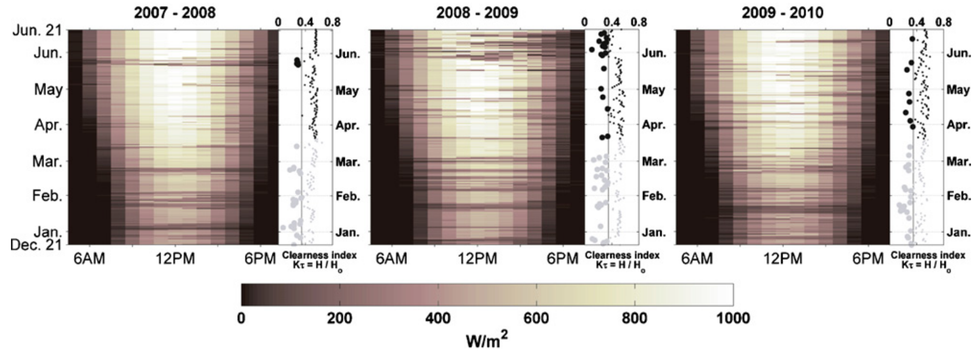

Fig. 6. Hourly global shortwave $R_{s\downarrow}$ radiation measured at the Topaz Lake meteorological station between the winter and summer solstices of water years 2008, 2009, and 2010. Daily clearness indices (K_τ) for each year are shown in the vertical scatter plots. Darkened data points indicate days after the spring equinox for each year. Circles (● symbols) indicate days when $K_\tau \leq 0.35$ (i.e. 'cloudy'); the vertical black line indicates this cloudy/clear sky threshold.

was computed for the period between the spring equinox and summer solstice of each year as

$$K_\tau = \frac{R_{S\downarrow}}{R_{S\downarrow,TOA}} \quad (2)$$

where $R_{S\downarrow,TOA}$ is the estimated horizontal solar flux received at the top of the atmosphere per unit area per hour, computed as Allen et al. (2006). Low (high) K_τ values represent low (high) radiation typically associated with cloudy (clear) sky conditions. However, no definitive thresholds exist by which to classify sky conditions based on K_τ (Okogbue et al., 2009). The threshold used to identify cloudy conditions varies by study from $K_\tau \leq 0.15$ (Okogbue et al., 2009) to $K_\tau \leq 0.35$ (Kuye and Jagtap, 1992). For this study, daily average K_τ was rarely less than 0.15 (Fig. 6). As a result, a threshold of $K_\tau \leq 0.35$ was specified to estimate cloudy conditions. Based on this K_τ threshold, 4, 23, and 8 days were categorized as cloudy in 2008, 2009, and 2010, respectively (Fig. 6).

3.4. Sub-canopy direct beam irradiance

An evaluation of the one-minute sub-canopy $R_{s\downarrow dir}$ at a single snow depth sensor location reveals the control of canopy structure on the transmission of the solar beam (Fig. 7). Periods of cloud cover are identifiable in the time series of the simulated sub-canopy direct beam flux; note the rapid transitions from red to blue in the vertical line graph in Fig. 7, indicating a shift in radiation dominance from the direct to diffuse light. Changes in daily average shortwave canopy transmission associated with temporally discontinuous cloud cover occur when clouds block the sun precisely when the direct beam would otherwise be transmitted through the canopy at a given location (Fig. 7; note changes in the vertical line graph during cloudy (blue) periods). Diurnal cross-sections of the sub-canopy direct beam irradiance on 1 March (lower) and 1 May (upper), 2008 illustrate the variability in sub-canopy solar beam irradiance relative to the above-canopy flux and general increase over the two-month period (Fig. 7; insets on right). The canopy transmission of the direct beam is therefore highly dynamic as a combined result of cloud cover and forest canopy structure coincident with the sky track of the sun (e.g. Fig. 4). The average daily probability (in percent likelihood) of *DBT* plotted in Fig. 5b was 12% and 37% in winter (21 December, 2007–21 March, 2008) and spring (21 March–21 June, 2008), respectively, while for the same two seasons the direct beam comprised 46% and 75%, respectively, of the total global sub-canopy solar irradiance. The results suggest that even in winter, despite the relatively low daily average probability of solar beam canopy transmittance, the direct beam still represented much of the sub-canopy solar irradiance.

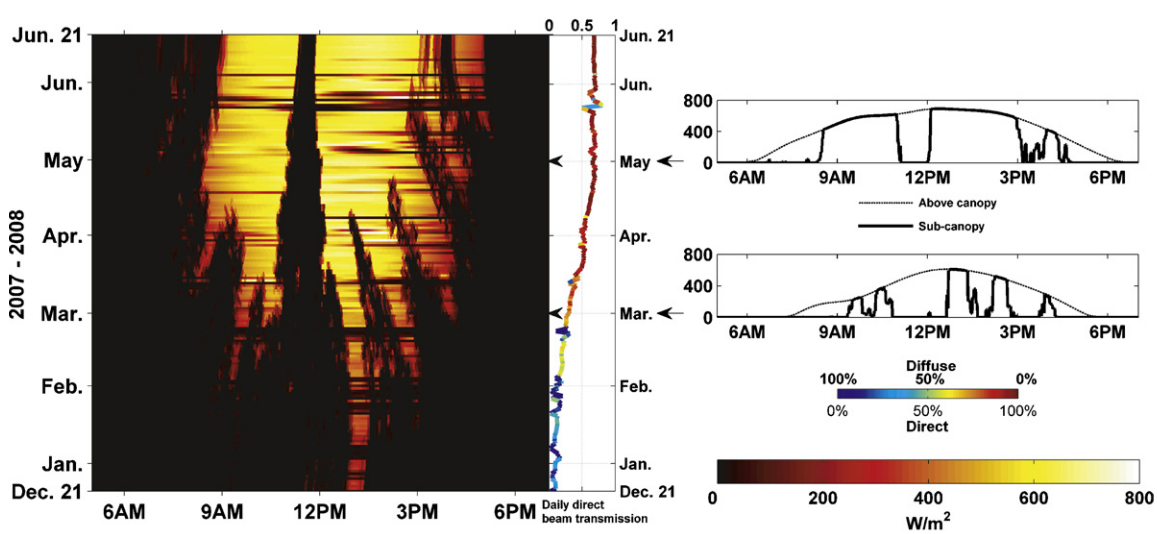

Fig. 7. Modeled sub-canopy $R_{s\downarrow dir}$ for 21 December, 2007–21 June, 2008 (left) at the same photo location shown in Fig. 4. The mean daily fraction of modeled sub-canopy to above-canopy direct beam irradiance (i.e. daily direct beam canopy transmission) is indicated by the vertical line graph and the daily fraction of total direct/diffuse irradiance is indicated by the line color. Diurnal examples of above-canopy (thin line) and sub-canopy (bold line) direct $R_{s\downarrow}$ for 1 March and 1 May, 2008 are included at right. (For interpretation of the references to color in this figure legend and in text, the reader is referred to the web version of this article.)

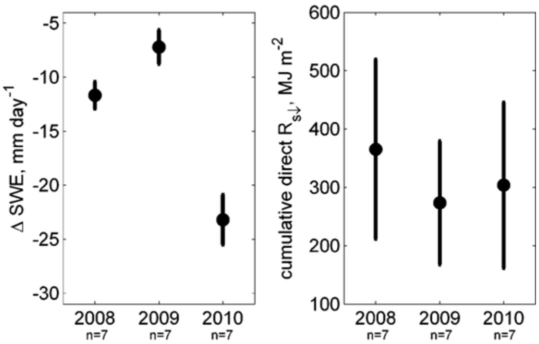

Fig. 8. Mean (● symbol) and standard deviation (error bars) of measured seasonal SWE ablation rates (left) and modeled cumulative melt season sub-canopy direct beam irradiance (right) for years 2008, 2009, and 2010. For consistent interannual comparison, only data from seven continuously operational sensor locations are shown.

The first validation of simulated $R_{s\downarrow dir}$ conducted for eight days and evaluated against data from three pyranometers yielded an average linear Pearson's correlation coefficient of 0.58 and a positive model bias of 9.9% was noted. The second validation experiment run at nine pyranometer locations for three days yielded an average correlation coefficient computed for the sub-canopy sensors and model estimates of 0.70 and a positive model bias of 7.1% was observed. Various error sources of the model and measurement designs likely contributed to the observed error and bias. Spatial offsets of as much as a few meters between the camera lens and pyranometer positions likely resulted in much of the observed error at the relatively high temporal resolution of the measurements and model estimates. The spatial offset between sensors and photographs effectively caused a temporal lag in the intermittent irradiance, reducing the correlation coefficient. The positive model bias could be attributed to a combination of error in the partition of above-canopy global radiation to direct and diffuse, hemispherical photo acquisition and analysis, and pyranometer measurement error at the base station (representing above-canopy) and/or the sub-canopy sensors. The potential influences of the various uncertainties on analyses and results are presented in Section 4.

3.5. Regression analyses

The mean ablation rates for the continuously operational snow depth sensors were −11.7 mm day^{-1}, −7.2 mm day^{-1}, and −23.2 mm day^{-1} in 2008, 2009, and 2010, respectively (Fig. 8). The mean cumulative sub-canopy direct beam irradiance from the date of maximum accumulation to the mean date of snow disappearance for the three years at the location of the continuously recording sensors was 365 MJ m^{-2} (23 March–29 May, 2008), 274 MJ m^{-2} (21 March–19 May, 2009), and 304 MJ m^{-2} (2 May–17 June, 2010) (Fig. 8). A total of 15, 12, and 19 sensors recorded SWE ablation rates in 2008, 2009, and 2010, respectively, and are used in the following regression analyses.

Generally, (negative) linear relationships were observed between seasonal SWE ablation (i.e. ΔSWE; with negative values indicating ablation) and modeled cumulative incident $R_{s\downarrow dir}$ (Fig. 9). The estimated cumulative direct beam irradiance explained 58%, 29%, and 23% of the variation in seasonal SWE ablation in 2008, 2009, and 2010, respectively. The linear relationship of the 2009 data was not statistically significant at the 5% level. Years with greater sub-canopy direct beam irradiance exhibited a stronger relationship between ablation rates and direct beam irradiance. Sky view factor exhibits the same general (negative) linear relationship with SWE ablation, but the slope and statistical significance of that relationship is dependent on the specified range of zenith angles used to compute SVF_θ. The sensitivity of the observed relationships between ablation rates and SVF_θ were evaluated for sensitivity to seasonal inter-annual differences in cloud cover for three years of record. Fig. 10 shows the coefficient of determination of the linear regression analyses conducted on the SWE ablation rates observed for each of the three years and SVF_θ computed over successively larger sky regions. The optimal zenith angle used to compute SVF_θ that resulted in the strongest correlation with ablation rates varied for each of the three years: 90° in 2009, the cloudiest season, and 45° (2010) and 66° (2008); years with less cloud cover and more direct beam irradiance (Fig. 10). The SVF_θ at these optimal zenith angles explained 41%, 87%, and 48% of the observed seasonal SWE ablation for the respective three years (Fig. 11).

4. Discussion

At least four factors likely contributed to the variability of observed SWE ablation rates. First and most importantly, cumulative sub-canopy direct beam irradiance was largely governed by the spatial arrangement of forest vegetation in the sky direction of the sun's path. Second, seasonal ablation rates are limited, in part, by the availability of incident solar irradiance, which varies seasonally with solar elevation. Hence, reduced ablation rates were observed at lower elevations (Fig. 9) where snowmelt commences earlier in the year when solar elevations are lower. At upper elevations snowmelt continues later into the year (Fig. 2) when solar

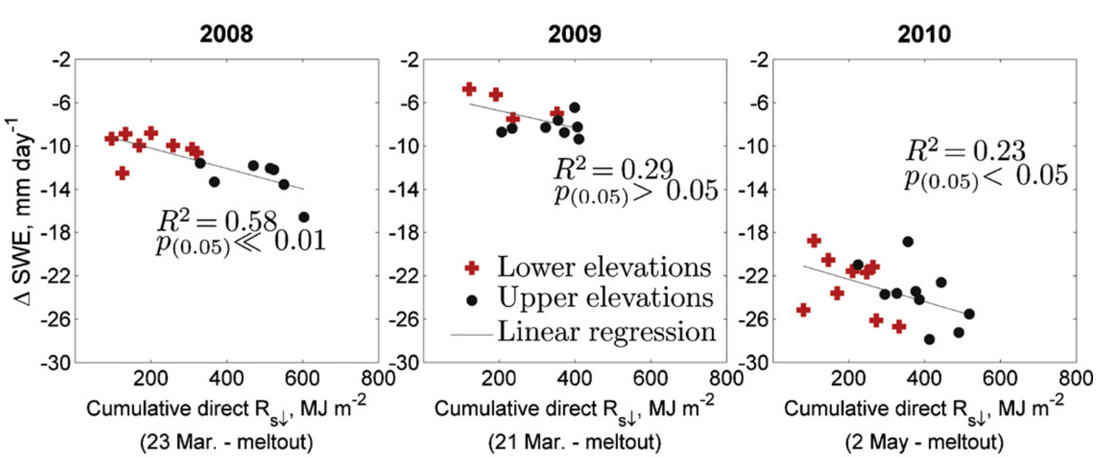

Fig. 9. Linear regression trends between spring SWE ablation rate measured at snow depth sensor locations and corresponding modeled cumulative seasonal sub-canopy shortwave irradiance for years 2008 (n = 15), 2009 (n = 12), and 2010 (n = 19).

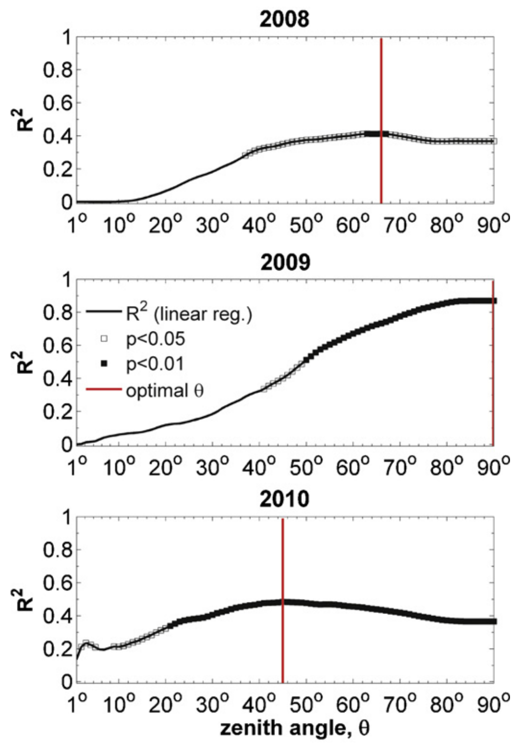

Fig. 10. Coefficient of determination and *p*-values from linear regression between seasonal SWE ablation (ΔSWE) measured at operational depth sensors for water years 2008, 2009, and 2010, and sky view factor (SVF_θ) at corresponding sensor locations computed by integrating canopy openness from specified zenith angles (1–90°) to nadir (0°). For each year, the vertical red line indicates the zenith angle that maximizes R^2 and minimizes the *p*-value. (For interpretation of the references to color in this figure legend, the reader is referred to the web version of this article.)

elevations are higher, resulting in greater seasonal ablation rates (Fig. 9). Third, snow ablation rates are governed by seasonal meteorology. Years with greater sub-canopy direct beam irradiance (and less cloud cover) exhibited a stronger relationship between seasonal ablation rates and direct beam irradiance (Fig. 9). While $R_{s\downarrow dir}$ explained nearly 60% of the observed variability in SWE ablation for the most cloud-free ablation season, the remaining unexplained variability for this year and for years with more cloud cover highlights the role of other energy sources known to drive plot-scale snowmelt variability. Finally, the timing of the melt season, defined by the period of time between peak SWE and snow disappearance, dictates the availability of incident solar radiation and thus strongly influences the SWE ablation rates. For example, the year with the latest peak SWE date (2 May, 2010) and latest mean snow disappearance date exhibited the shortest melt season duration (see Table 2). In contrast, 2008 was the clearest melt season on record but, with a peak SWE date of 23 March, recorded the longest melt season duration of the three years despite recording only ∼74% of the 2010 peak SWE. Other inter-annual meteorological differences during the melt season such as air temperature, snowfall, humidity, wind, cloud cover and rain-on-snow events would also be expected to result in inter-annual differences in seasonal SWE ablation rates.

Numerous sources of uncertainty could potentially complicate the statistical relationships between seasonal SWE ablation rates and the metrics direct beam irradiance and SVF_θ. How these error sources influence the interpreted results depend on the type and degree of uncertainty and the methods available to minimize the errors. For example, the geo-reference errors in hemispherical photos can be minimized by following documented methods (e.g. Frazer et al., 1999; Hardy et al., 2004). Such errors would be expected to be small and relatively random in nature. Conversely, errors associated with the use of radiation measurements made in an alpine area 8 km from the study site to represent above-canopy radiation at lower elevations may have greater implications on the results. For example, a three-year comparison of $R_{s\downarrow}$ measured at Topaz Lake and a station 340 m lower in elevation than the study area yielded a correlation coefficient of 0.93. Despite the relatively high long-term correlation, the correlation was lower during cloudy periods, indicating that the alpine region experienced more cloud cover than the lower elevations.

The use of these data to represent above-canopy global solar radiation at the lower elevations could introduce a negative bias in the radiation data, particularly during cloudy periods. This bias could potentially influence inter-annual comparisons and interpretations of the results. A bias would be expected to manifest largely during the cloudiest season (e.g. 2009) and would decrease the significance of the linear regression between ablation rates and direct beam solar irradiance for this year. A simple test for this radiative bias would be to examine the zenith angle that resulted in the best linear fit between seasonal SWE ablation rates and SVF_θ. A negative radiation bias (i.e. simulating cloudy conditions when it is actually clear) would cause a decrease in the 'optimal' zenith angle, similar to what is observed during years with less cloud cover (e.g. 2008 and 2010). The optimal zenith angle of 90° during the 2009 melt season suggests that this potential radiation bias was negligible (i.e. measured cloud cover in the alpine similarly impacted the Wolverton basin).

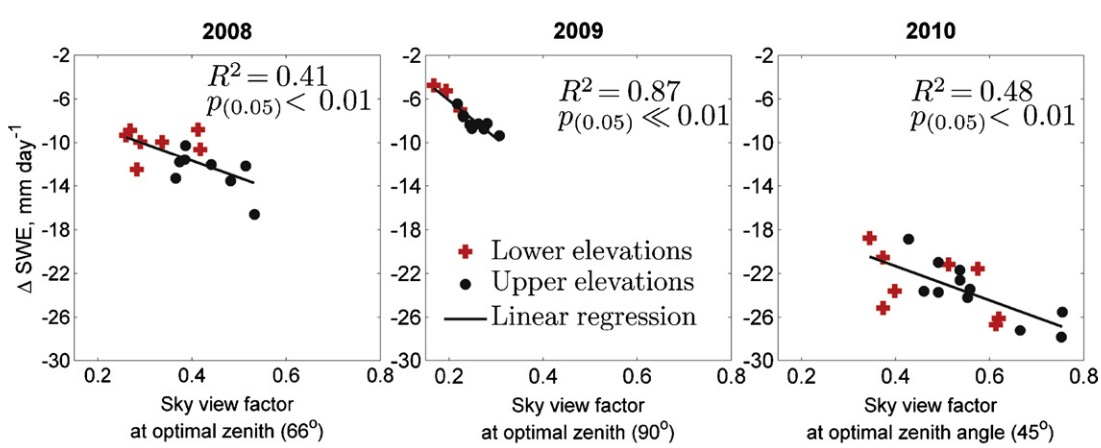

Fig. 11. Linear regression trends between seasonal SWE ablation rates shown in Fig. 9 and the corresponding measured SVF_θ at the optimal zenith angles for years 2008 ($n = 15$), 2009 ($n = 12$), and 2010 ($n = 19$) as indicated by the red lines in Fig. 10.

The strength of the statistical relationship between sky view (a measure of canopy openness) and observed ablation was found to be sensitive to the concentric area of the hemispherical sky view used to evaluate SVF_θ. The findings support results of López-Moreno and Latron (2008), in which a sensitivity between SWE, time of year, and the specified range of zenith angles used to compute SVF_θ was documented. Evaluation of the zenith angle that when used to compute SVF_θ explains the most variability in ablation rates across all snow depth sensor locations may provide insight into the source of the governing energy fluxes. For example, the high optimal zenith angle of 90° predicted during the cloudiest melt season suggests the dominance of energy sources derived from all hemispherical directions, including diffuse radiation and atmospheric and terrestrial longwave radiation known to be dominant energy fluxes during cloudy conditions. The reduced optimal zenith angles for years with less cloud cover and/or a later melt season imply a stronger influence of the solar direct beam with respect to the sub-canopy energy balance. For example, the daytime average and average daily maximum solar zenith angles during the melt season were 53° and 25° in 2008 (March 23–May 22) and were 50° and 16° in 2010 (May 2–June 16). The zenith angle at which SVF_θ explained the most variability in ablation rates of 45° in 2010 (8 cloudy days and late melt season) is close to the 50° daily average solar zenith angle for this melt season. In 2008 (four cloudy days and early melt season), the optimal SVF_θ zenith angle of 66° is nearer to the horizon than the 53° daily average solar zenith angle. The differences suggest that the variability of ablation rates during the earlier melt season (i.e. 2008) may be less impacted by direct beam solar irradiance than the melt season that occurred later (i.e. 2010) despite the latter season experiencing more cloud cover. The results indicate that the ability of the individual metrics to explain observed variability in SWE ablation rates is related to seasonal meteorology (i.e. both cloud cover and timing and duration of the melt season). Combined, the two metrics studied here (sub-canopy direct beam irradiance and SVF_θ) may be used to explain much of the observed plot-scale variability in SWE ablation at the finer time scales relevant to snow and hydrological model applications.

Land surface and hydrological models typically use spatially aggregated (i.e. bulk) representations of complex, three-dimensional (3-D) canopy structure to represent the numerous mechanisms known to cause spatiotemporal variability in SWE. Satellite-derived estimates of canopy density and LAI' are two bulk forest metrics commonly used to scale above-canopy fluxes to the sub-canopy surface. Despite well-documented relationships between sub-canopy fluxes and area-averaged LAI' and canopy density, these bulk metrics often lack the level of detail necessary to fully explain sub-canopy snow dynamics (Varhola et al., 2010b). Essery et al. (2008b) suggest that a more explicit characterization of canopy structure is needed to resolve the distribution of sub-canopy energetics and snow cover depletion. Detailed atmosphere – canopy radiative transfer models have proven accurate in the simulation of forest light environments for the estimation of photosynthesis and carbon sequestration (Kobayashi and Iwabuchi, 2008), but the distributed application of such techniques is generally limited by computational expense and data requirements. An effective compromise in detailed canopy representation may split the difference between bulk forest metrics such as LAI' or canopy density and 3-D canopy structure data required by multispectral radiative transfer models.

The metrics SVF_θ and direct beam irradiance could be combined with other variables such as canopy parameters, slope, aspect or elevation to further explain variability of observed ablation rates. However, the relationships and metrics explored in this study have more global implications for the improvement of land surface and hydrologic models in snow-covered forests. For example, direct beam canopy transmissivity could be incorporated as a time-variant model input rather than using bulk LAI′ and extinction parameter values in a Beer's-type exponential reduction of above-canopy direct beam solar radiation. Similarly, SVF_θ determined at optimal zenith angles defining sky/canopy regions that most influence particular energy fluxes could be used to simulate energy fluxes that are more omni-directional than the solar direct beam. For example, SVF_θ determined from hemispherical photographs could be used to estimate sub-canopy longwave irradiance during cloudy periods. However, during clear sky conditions the added contribution of longwave radiation by sunlit canopy elements (e.g. Pomeroy et al., 2009) introduces a third dimension to the problem that cannot be fully addressed with a single two-dimensional photograph. Increasingly available light detection and ranging (LiDAR) data provide a means to obtain these and other canopy structure metrics for future basin-scale hydrological applications.

Terrestrial LiDAR techniques have been used to estimate *directional SVF* (e.g. Côté et al., 2009; Danson et al., 2007) but, like hemispherical photography, the technique is limited in its application at hydrologically relevant scales (i.e. catchment level). Toward bridging this scale gap, airborne scanning LiDAR systems offer an innovative alternative (van Leeuwen and Nieuwenhuis, 2010; Varhola et al., 2010a) to other indirect methods in that they capture the general spatial arrangement and structure of vegetation over large areas. Work by Essery et al. (2008a) to derive a view shed of surrounding forest vegetation from an orthophoto and LiDAR data shows promise for subsequent distributed applications of the current work. Future efforts will explore the utility of detailed canopy metrics to improve the representation of surface–atmosphere interactions in physically based snow, hydrological, and ecological models, including extending the presented methods to estimate the sub-canopy thermal radiative environment. Efforts will include the use of LiDAR data to map the most physically meaningful, detailed canopy metrics over large areas for distributed model application.

5. Conclusions

Sub-canopy cumulative seasonal direct beam solar irradiance derived from above-canopy measurements and hemispherical photography explained the most variability in snow ablation rates during the least cloudy melt season (58%, $p_{(0.05)} \ll 0.01$; 2008; 4 cloudy days, 365 MJ m^{-2} direct irradiance), less for the snowmelt season with intermediate cloud cover (23%, $p_{(0.05)} < 0.05$; 2010; 8 cloudy days, 304 MJ m^{-2} direct irradiance), and the least during the cloudiest melt season of the study (29%, $p_{(0.05)} > 0.05$; 2009; 23 cloudy days, 274 MJ m^{-2} direct irradiance). Conversely, sky view factor (SVF_θ) explained the most variability in snow ablation rates under cloudier conditions (i.e. 87% in 2009, $p_{(0.05)} \ll 0.01$) and the relationships between SVF_θ and ablation rates were stronger when developed over the entire hemisphere (i.e. SVF_{90°). Combined, the two metrics studied here (sub-canopy direct beam irradiance and SVF_θ) may be used to explain much of the observed plot-scale variability in SWE ablation at finer time scales relevant to physically based snow and hydrological model applications.

Acknowledgments

The authors thank Sequoia National Park for access rights and continued support of ongoing research efforts. Financial support was provided by the National Science Foundation grants EAR-071160, EAR-1032295, EAR-1032308, the Southern Sierra Critical Zone Observatory (EAR-0725097), a Major Research Instrumentation grant (EAR-0619947), the Mountain Research Initiative, and a National Aeronautics and Space Administration (NASA) Earth System Science Fellowship. J. Melack and J. Sickman provided valuable solar radiation data from the Tokopah basin. The authors are grateful to everyone who provided assistance in the field and office including: B. Forman, D. Perrot, S. Roberts, D. Berisford, E. Trujillo, L. Meromy, M. Girotto, and M. Cooper, among many others.

References

Allen, R.G., Trezza, R., Tasumi, M., 2006. Analytical integrated functions for daily solar radiation on slopes. Agricultural and Forest Meteorology 139 (1–2), 55–73.
Baldocchi, D.D., Matt, D.R., Hutchison, B.A., McMillen, R.T., 1984. Solar radiation within an oak – hickory forest: an evaluation of the extinction coefficients for several radiation components during fully-leafed and leafless periods. Agricultural and Forest Meteorology 32 (3–4), 307–322.
Bales, R.C., Hopmans, J., O'Geen, T.O., Meadows, M., Hartsough, P.C., Kirchner, P., Hunsaker, C.T., Beaudette, D., 2011. Soil moisture response to snowmelt and rainfall in a Sierra Nevada mixed-conifer forest. Vadose Zone Journal 10, 786–799.
Becker, P., Erhart, D.W., Smith, A.P., 1989. Analysis of forest light environments. Part I. Computerized estimation of solar radiation from hemispherical canopy photographs. Agricultural and Forest Meteorology 44 (3–4), 217–232.
Côté, J.-F., Widlowski, J.-L., Fournier, R.A., Verstraete, M.M., 2009. The structural and radiative consistency of three-dimensional tree reconstructions from terrestrial lidar. Remote Sensing of Environment 113 (5), 1067–1081.
Danson, F.M., Hetherington, D., Morsdorf, F., Koetz, B., Allgower, B., 2007. Forest canopy gap fraction from terrestrial laser scanning. Geoscience and Remote Sensing Letters, IEEE 4 (1), 157–160.
Ellis, C.R., Pomeroy, J.W., 2007. Estimating sub-canopy shortwave irradiance to melting snow on forested slopes. Hydrological Processes 21 (19), 2581–2593.
Essery, R., Bunting, P., Rowlands, A., Rutter, N., Hardy, J.P., Melloh, R., Link, T.E., Marks, D., Pomeroy, J.W., 2008a. Radiative transfer modeling of a coniferous canopy characterized by airborne remote sensing. Journal of Hydrometeorology 9, 228–241.
Essery, R., Pomeroy, J., Ellis, C., Link, T., 2008b. Modelling longwave radiation to snow beneath forest canopies using hemispherical photography or linear regression. Hydrological Processes 22 (15), 2788–2800.
Essery, R.L., Pomeroy, J.W., Parvianen, J., Storck, P., 2003. Sublimation of snow from coniferous forests in a climate model. Journal of Climate 16, 1855–1864.
Faria, D.A., Pomeroy, J.W., Essery, R.L.H., 2000. Effect of covariance between ablation and snow water equivalent on depletion of snow-covered area in a forest. Hydrological Processes 14 (15), 2683–2695.
Frazer, G.W., Canham, C.D., Lertzman, K.P., 1999. Gap Light Analyser (GLA). Version 2.0: Imaging Software to Extract Canopy Structure and Gap Light Transmission Indices from True-Colour Fisheye Photographs. Users Manual and Program Documentation. Simon Fraser University, Burnaby, B.C. and the Institute of Ecosystem Studies, Millbrook, New York.
Frazer, G.W., Trofymow, J.A., Lertzman, K.P., 2000. Canopy openness and leaf area in chronosequences of coastal temperate rainforests. Canadian Journal of Forest Research 30 (2), 239–256.
Golding, D.L., Swanson, R.H., 1986. Snow distribution patterns in clearings and adjacent forest. Water Resources Research 22 (13), 1931–1940.
Hardy, J.P., Melloh, R., Koenig, G., Marks, D., Winstral, A., Pomeroy, J.W., Link, T.E., 2004. Solar radiation transmission through conifer canopies. Agricultural and Forest Meteorology 126 (3–4), 257–270.
Hedstrom, N.R., Pomeroy, J.W., 1998. Measurements and modelling of snow interception in the boreal forest. Hydrological Processes 12 (10–11), 1611–1625.
Homer, C., Huang, C., Yang, C., Wylie, B., Coan, M., 2004. Development of a 2001 National Landcover Database for the United States. Photogrammetric Engineering and Remote Sensing 70, 829–840.
Kittredge, J., 1953. Influences of forests on snow in ponderosa—sugar pine fir zone of the central Sierra Nevada. Hilgardia 22 (1), 1–96.
Kobayashi, H., Iwabuchi, H., 2008. A coupled 1-D atmosphere and 3-D canopy radiative transfer model for canopy reflectance, light environment, and photosynthesis simulation in a heterogeneous landscape. Remote Sensing of Environment 112 (1), 173–185.
Koivusalo, H., Kokkonen, T., 2002. Snow processes in a forest clearing and in a coniferous forest. Journal of Hydrology 262 (1–4), 145–164.
Kuye, A., Jagtap, S.S., 1992. Analysis of solar radiation data for Port Harcourt, Nigeria. Solar Energy 49 (2), 139–145.
Lehning, M., Bartelt, P., Brown, B., Fierz, C., 2002. A physical SNOWPACK model for the Swiss avalanche warning. Part III: meteorological forcing, thin layer formation and evaluation. Cold Regions Science and Technology 35 (3), 169–184.
Link, T.E., Marks, D., 1999. Point simulation of seasonal snow cover dynamics beneath boreal forest canopies. Journal of Geophysical Research 104 (D22), 27841–27857.
Liston, G.E., 1995. Local advection of momentum, heat, and moisture during the melt of patchy snow covers. Journal of Applied Meteorology 34 (7), 1705–1715.
Liu, Y.H., Jordan, R.C., 1960. The interrelationship and characteristic distribution of direct, diffuse and total solar radiation. Solar Energy 4 (3), 1–19.
López-Moreno, J.I., Latron, J., 2008. Influence of canopy density on snow distribution in a temperate mountain range. Hydrological Processes 22 (1), 117–126.
López-Moreno, J.I., Stähli, M., 2008. Statistical analysis of the snow cover variability in a subalpine watershed: assessing the role of topography and forest interactions. Journal of Hydrology 348 (3–4), 379–394.
Lundberg, A., Calder, I., Harding, R., 1998. Evaporation of intercepted snow: measurement and modelling. Journal of Hydrology 206 (3–4), 151–163.
Molotch, N.P., Blanken, P.D., Link, T.E., 2011. Snow: hydrological and ecological feedbacks in forests. In: Levia, D.F., Carlyle-Moses, D., Tanaka, T. (Eds.), Forest Hydrology and Biogeochemistry. Ecological Studies. Springer, Netherlands, pp. 541–555.
Molotch, N.P., Brooks, P.D., Burns, S.P., Litvak, M., Monson, R.K., McConnell, J.R., Musselman, K.N., 2009. Ecohydrological controls on snowmelt partitioning in mixed-conifer sub-alpine forests. Ecohydrology 2 (2), 129–142.
Musselman, K.N., Molotch, N.P., Brooks, P.D., 2008. Effects of vegetation on snow accumulation and ablation in a mid-latitude sub-alpine forest. Hydrological Processes 22 (15), 2767–2776.
Norman, J.M., Campbell, G.S., 1989. Plant physiological ecology field methods and instrumentation. In: Pearcy, R.W., et al. (Eds.), Canopy Structure. Chapman and Hall, London, pp. 301–325.
Oke, T.R., 1988. Boundary Layer Climates. Routledge (formerly Methuen), New York, NY (USA).
Okogbue, E.C., Adedokun, J.A., Holmgren, B., 2009. Hourly and daily clearness index and diffuse fraction at a tropical station, Ile-Ife, Nigeria. International Journal of Climatology 29 (8), 1035–1047.
Pomeroy, J.W., Dion, K., 1996. Winter radiation extinction and reflection in a boreal pine canopy: measurements and modelling. Hydrological Processes 10 (12), 1591–1608.
Pomeroy, J.W., Gray, D.M., Hedstrom, N.R., Janowicz, J.R., 2002. Prediction of seasonal snow accumulation in cold climate forests. Hydrological Processes 16 (18), 3543–3558.
Pomeroy, J.W., Hanson, S., Faria, D., 2001. Small-scale variation in snowmelt energy in a boreal forest: an additional factor controlling depletion of snow cover? In: 58th Eastern Snow Conference, Ottawa, Ontario, Canada.
Pomeroy, J.W., Marks, D., Link, T.E., Ellis, C., Hardy, J.P., Rowlands, A., Granger, R., 2009. The impact of coniferous forest temperature on incoming longwave radiation to melting snow. Hydrological Processes 23 (17), 2513–2525.
Price, A.G., Dunne, T., 1976. Energy balance computations of snowmelt in a subarctic area. Water Resources Research 12 (4), 686–694.
Reda, I., Andreas, A., 2004. Solar position algorithm for solar radiation applications. Solar Energy 76 (5), 577–589.
Rutter, N., Essery, R., Pomeroy, J., Altimir, N., Andreadis, K., Baker, I., Barr, A., Bartlett, P., Boone, A., Deng, H., Douville, H., Dutra, E., Elder, K., Ellis, C., Feng, X., Gelfan, A., Goodbody, A., Gusev, Y., Gustafsson, D., Hellström, R., Hirabayashi, Y., Hirota, T., Jonas, T., Koren, V., Kuragina, A., Lettenmaier, D., Li, W., Luce, C., Martin, E., Nasonova, O., Pumpanen, J., Pyles, R., Samuelsson, P., Sandells, M., Schädler, G., Shmakin, A., Smirnova, T.G., Stähli, M., Stöckli, R., Strasser, U., Su, H., Suzuki, K., Takata, K., Tanaka, K., Thompson, E., Vesala, T., Viterbo, P., Wiltshire, A., Xia, K., Xue, Y., Yamazaki, T., 2009. Evaluation of forest snow processes models (SnowMIP2). Journal of Geophysical Research-Atmospheres 114, D06111.
Schleppi, P., 2011. Forested water catchments in a changing environment. In: Bredemeier, M., et al. (Eds.), Forest Management and the Water Cycle. Ecological Studies. Springer, Netherlands, pp. 89–110.
Schleppi, P., Conedera, M., Sedivy, I., Thimonier, A., 2007. Correcting non-linearity and slope effects in the estimation of the leaf area index of forests from hemispherical photographs. Agricultural and Forest Meteorology 144 (3–4), 236–242.
Sicart, J.E., Pomeroy, J.W., Essery, R.L.H., Hardy, J.P., Link, T.E., Marks, D., 2004. A sensitivity study of daytime net radiation during snowmelt to forest canopy and atmospheric conditions. Journal of Hydrometeorology 5 (5), 774–784.
Stähli, M., Jonas, T., Gustafsson, D., 2009. The role of snow interception in winter-time radiation processes of a coniferous sub-alpine forest. Hydrological Processes 23 (17), 2498–2512.
Storck, P., Lettenmaier, D.P., Bolton, S.M., 2002. Measurement of snow interception and canopy effects on snow accumulation and melt in a mountainous maritime climate, Oregon, United States. Water Resources Research 38 (11), 1223.
Talbot, J., Plamondon, A.P., Lévesque, D., Aubé, D., Prévos, M., Chazalmartin, F., Gnocchini, M., 2006. Relating snow dynamics and balsam fir stand characteristics, Montmorency Forest, Quebec. Hydrological Processes 20 (5), 1187–1199.
van Leeuwen, M., Nieuwenhuis, M., 2010. Retrieval of forest structural parameters using LiDAR remote sensing. European Journal of Forest Research 129 (4), 749–770.
Varhola, A., Coops, N.C., Bater, C.W., Teti, P., Boon, S., Weiler, M., 2010a. The influence of ground- and lidar-derived forest structure metrics on snow accumulation and ablation in disturbed forests. Canadian Journal of Forest Research 40, 812–821.
Varhola, A., Coops, N.C., Weiler, M., Moore, R.D., 2010b. Forest canopy effects on snow accumulation and ablation: an integrative review of empirical results. Journal of Hydrology 392 (3–4), 219–233.
Veatch, W., Brooks, P.D., Gustafson, J.R., Molotch, N.P., 2009. Quantifying the effects of forest canopy cover on net snow accumulation at a continental, mid-latitude site. Ecohydrology 2 (2), 115–128.